Strain and luminescence properties of hexagonal hillocks in N-polar GaN

Jochen Bruckbauer ✉ 📧 ; Grzegorz Cios 📧 ; Andrei Sarua 📧 ; Peng Feng 📧 ; Tao Wang 📧 ;
Ben Hourahine 📧 ; Aimo Winkelmann 📧 ; Carol Trager-Cowan 📧 ; Robert W. Martin 📧

Check for updates

View Online

Export Citation

Articles You May Be Interested In

Luminescence behavior of semipolar (10 1 ̄ 1) InGaN/GaN "bow-tie" structures on patterned Si substrates

J. Appl. Phys. (January 2020)

A transmission electron microscopy study of hillocks in thin aluminum films

J. Vac. Sci. Technol. B (January 1991)

Origin of pyramidal hillocks on GaN thin films grown on free-standing m -plane GaN substrates

Appl. Phys. Lett. (June 2010)

Strain and luminescence properties of hexagonal hillocks in N-polar GaN

View Online   Export Citation   CrossMark

Jochen Bruckbauer,[1,a)] ⓘ Grzegorz Cios,[2] ⓘ Andrei Sarua,[3] ⓘ Peng Feng,[4] ⓘ Tao Wang,[5] ⓘ Ben Hourahine,[1] ⓘ Aimo Winkelmann,[1,2] ⓘ Carol Trager-Cowan,[1] ⓘ and Robert W. Martin[1] ⓘ

AFFILIATIONS

[1]Department of Physics, SUPA, University of Strathclyde, Glasgow G4 0NG, Scotland, United Kingdom
[2]Academic Centre for Materials and Nanotechnology, AGH University of Krakow, 30-059 Kraków, Poland
[3]HH Wills Physics Laboratory, School of Physics, University of Bristol, Bristol BS81TL, United Kingdom
[4]Department of Electronic and Electrical Engineering, University of Sheffield, Sheffield S1 3JD, United Kingdom
[5]School of Physics and Astronomy, Cardiff University, Cardiff CF24 3AA, United Kingdom

[a)]Author to whom correspondence should be addressed: jochen.bruckbauer@strath.ac.uk

ABSTRACT

Owing to its unique properties, N-polar GaN offers several advantages over Ga-polar GaN, particularly for applications in high power electronics. However, the growth of high-quality N-polar material is challenging. One dominant issue is the increased surface roughness, due to the occurrence of hexagonal-shaped hillocks, referred to as hexagons, on the material's surface. Although there are different methods to reduce the density of these hillocks, such as the use of vicinal substrates or optimum growth conditions, the properties of such hillocks are not extensively studied. Here, we investigate the crystallographic and luminescence properties of these hexagonal features using the techniques of electron backscatter diffraction (EBSD) and cathodoluminescence (CL) hyperspectral imaging in the scanning electron microscope combined with micro-Raman mapping. CL revealed increased light emission from the top of the hexagons compared with the surrounding material. Additionally, dark spots in intensity images, associated with non-radiative recombination at threading dislocations, could be resolved on top of the hexagons, but not in the surrounding area, implying improved material quality of the hexagons. Extensive strain analysis using EBSD revealed that the hexagons are composed of equivalent triangular segments with tensile strain along symmetrically equivalent $\langle 11\bar{2}0 \rangle$ directions. As the hexagons become larger, this strain increases with the distance from the center. This was confirmed by mapping the Raman E_2 (high) mode. Overall, this provides crucial insight into the strain state of these hexagonal features.

I. INTRODUCTION

III-nitride semiconductors, such as GaN, AlN, and their alloys, are hugely successful in optoelectronic devices, such as light-emitting diodes (LEDs) and laser diodes, and high power and high frequency electronics, such as high electron mobility transistors (HEMTs), due to their versatile properties. Nitrides exhibit a crystal polarity along the c-axis due to a lack of inversion symmetry of the hexagonal wurtzite crystal structure (space group: $P6_3mc$ or 186; point group: $6mm$) in this direction. This leads to spontaneous polarization fields along the c-axis. GaN grown along the $+c$-direction (or (0001), Ga-polar) and $-c$-direction (or (000$\bar{1}$), N-polar) exhibits different surface, structural, optical, and electrical properties.[1–3] Polarity affects devices differently depending on their type. For light emitters, such as LEDs, polarity is generally detrimental to the device performance. In contrast, for HEMTs, polarity is exploited to create a two-dimensional electron gas (2DEG). Specifically, N-polar HEMTs are desirable as they offer enhanced electron confinement, promise improved performance, and improve device scalability compared to Ga-polar devices.[4,5]

Commonly, GaN is grown along the $+c$-direction. The growth along the $-c$-direction presents challenges as described in the following. N-polar GaN generally exhibits poor crystal quality, such as increased surface roughness, increased dislocation density, and the occurrence of hexagonal hillocks, here referred to as hexagons.[6–10]

09 April 2025 10:30:37

These hexagons occur regardless of the substrate used and have been observed for growth on native bulk GaN and foreign substrates, such as sapphire and SiC.[9,11,12] The observed increased surface roughness is associated with the presence of these hillocks. There are several routes that allow the suppression of hillocks. These include the use of vicinal substrates, i.e., substrates with a slight off-cut up to 4°, which increases step flow growth.[11,13] Additionally, N-polar GaN layers with decreased surface roughness can be achieved through the control of the growth temperature, V/III ratio, and the use of indium surfactants during the growth.[10,12,14–16]

The growth of N-polar orientated GaN can be induced by different methods, for example, pre-treatment (nitridation) of the sapphire substrate at high temperature before growth, use of suitable polarity of the substrate (e.g., carbon-face of SiC), or selecting the appropriate growth conditions of the nucleation layer.[2,3,13,17,18]

Different growth conditions have been explored to further improve the material quality and reduce impurity incorporation and decrease threading dislocation density, such as changes in the V/III ratio, use of hydrogen during the growth, or lateral overgrowth.[12,14,16,19,20] However, additional challenges still remain for N-polar GaN, such as the increased incorporation of impurities, predominantly carbon and oxygen, and the occurrence of polarity inversion domains.[8,21]

In this paper, we investigate hexagonal hillocks in N-polar GaN using the techniques of cathodoluminescence (CL) imaging, micro-Raman imaging, and electron backscatter diffraction (EBSD) to correlate their light emission and strain properties.

II. MATERIALS AND METHODS

The N-polar GaN epilayers were grown by metal-organic vapor-phase epitaxy (MOVPE) on c-plane sapphire substrates. First, the N-polar GaN was induced by high temperature nitridation at 1150 °C in an environment of ammonia and H_2, this was followed by the growth of a low temperature GaN nucleation layer at 525 °C of about 25 nm thickness. Finally, a 900 nm thick N-polar layer was grown at 1150 °C.

EBSD was performed with a field emission gun scanning electron microscope (SEM) using either an Oxford Instruments Nordlys EBSD system (on a FEI Quanta 250) or a Symmetry S2 EBSD detector (on a FEI Versa 3D DualBeam). Initial indexing was performed using Oxford Instruments' Hough transform-based Refined Accuracy method. Further orientation refinement was carried out by pattern matching where each experimental electron backscatter pattern (EBSP) is compared with a dynamically simulated EBSP.[22,23] Afterward, the EBSD data were analyzed using MTEX, a MATLAB-based toolbox.[24] Elastic strain analysis was performed using the cross-correlation-based method of high angular resolution EBSD (HR-EBSD) using CrossCourt 4.[25,26] All EBSD measurements were performed at a sample tilt of 70° and an electron beam voltage of 20 kV; the pattern sizes were $1344 \times 1024 \, px^2$ (Nordlys EBSD data) or $1244 \times 1024 \, px^2$ (Symmetry S2 data).

CL hyperspectral imaging was performed on the FEI Quanta SEM using a custom-built system with the sample tilted at 45°.[27,28] The light is collected using a Schwarzschild reflecting objective with its optical axis 90° to the incident electron beam, dispersed using a 1/8 m focal length spectrometer (Oriel MS125), and detected with an 1600-channel electron multiplying charged-coupled device (Andor Newton EMCCD). All CL data were collected at an acceleration voltage of 5 kV and at room temperature. The hyperspectral data were recorded and analyzed using bespoke software and the images were generated by either plotting intensity images of a selected wavelength range or plotting peak parameters from least-square peak fitting, such as peak position (energy) or peak height (intensity).

Raman spectroscopy measurements were performed at room temperature using a Renishaw Invia spectrometer and a 488 nm solid-state laser. The laser beam was focused on the sample surface using a 100× microscope lens (NA = 0.9) to a spot of ≈0.5 μm in diameter. The unpolarized signal was collected in a confocal mode in the quasi-backscattering geometry. The sample probing depth is around ≈2 μm and is comparable with the total thickness of the GaN layer/hexagons, so the Raman information represents a depth average of the total film thickness. The sample was mounted on an automated XYZ microscope stage allowing scanning with ≈0.05 μm step resolution in the XY-plane. Raman images were obtained from peak fitting of the E_2 (high) phonon mode in GaN at each measured location to extract peak position, total peak area, and peak full width at half maximum (FWHM). The A_1 (LO) phonon mode was also visible for this orientation in GaN, but the signal was very weak and broad.

III. RESULTS AND DISCUSSION

The luminescence properties of the N-polar GaN epilayer and the hexagonal hillocks present on the sample surface were investigated using CL imaging over varying length scales. Figure 1(a) displays a secondary electron (SE) image of an entire hexagon and its planar surrounding area. Two smaller areas of the same size are marked, one on top of the hexagon near its center and another region in the adjacent area next to the hexagonal feature with the respective SE images shown in Figs. 1(b) and 1(c). CL imaging was carried out in all three areas with varying step sizes in order to investigate the emission across an entire hexagon and its surrounding area as well as to resolve the emission on smaller length scales on top of and next to the hexagon.

From the SE image in Fig. 1(a), it can be observed that the hexagon is raised compared with its surrounding region and has sloping sidewalls along the m-direction. The shape of the hexagons was confirmed using atomic force microscopy (AFM), as shown in Fig. S1 in the supplementary material. Overall, the light emission from the hexagon is much stronger compared with its surrounding area. Two emission peaks were observed, namely, the GaN near band edge (NBE) emission around 365 nm and the defect-related yellow band (YB) emission around 560 nm and their CL integrated intensity maps are shown in Figs. 1(d) and 1(g), respectively. Both the GaN NBE emission as well as the yellow band emission are about one order of magnitude larger on top of the hexagon than the area surrounding it. It can also be observed in both CL integrated intensity images that there is increased emission along lines in the a-direction, visible as brighter lines separating the six triangular segments of the hexagonal feature.
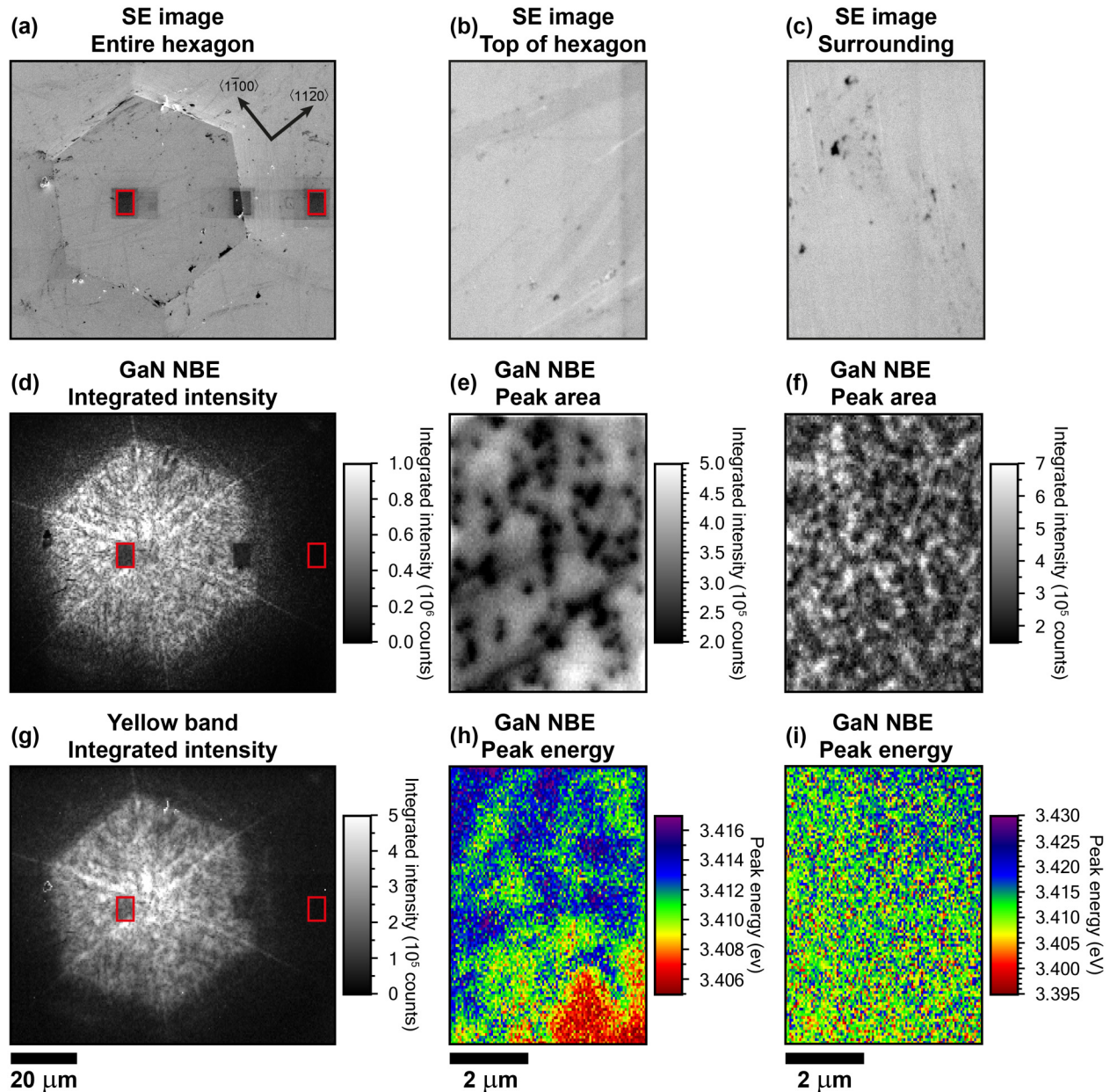
FIG. 1. CL hyperspectral imaging: (a) SE image, (d) and (g) CL integrated intensity image of the GaN NBE emission (350–380 nm) and of the yellow band emission (500–650 nm) of an entire hexagon and its surrounding area, respectively. (b) SE image, (e) CL peak area, and (h) CL peak energy image taken from the top of the hexagon. (c) SE image, (f) CL peak area, and (i) CL peak energy image taken from the surrounding area adjacent to the hexagon. The smaller areas on top and next to the hexagon are marked by the red boxes in the SE image in (a). They appear darker because the small regions were imaged before the large area measurement. All images in a column have the same spatial scale bar as shown at the bottom.

A higher resolution CL dataset was recorded from the region near the center of the hexagon, as seen in the SE image in Fig. 1(b). The GaN NBE peak was fitted using a Voigt function and the GaN peak area, and peak energy images are displayed in Figs. 1(e) and 1(h), respectively. The peak area or intensity image [Fig. 1(e)] shows the usual dark spots that are commonly observed in GaN epilayers and associated with non-radiative recombination at dislocations threading to the sample surface.[29,30] Some dislocations can

be individually resolved, whereas others in different regions are closer together. Variations in the NBE peak energy, observed around the dislocations as seen in Fig. 1(h), are of the order of 10 meV. They are either caused by local strain gradients[31–33] or by a change in impurity incorporation around dislocations leading to a varying bandgap.[34,35] Overall, the CL images show typical optical behavior for a GaN thin film.

The area surrounding the hexagonal features on the other hand is different. The CL intensity image in Fig. 1(f) shows a very high density of small dark spots, which are not clearly resolved. This implies that a very high density of defects is present in this region. This is supported by the strongly reduced emission intensity compared with the intensity at the top of the hexagon as seen in Fig. 1(d). No discernible impact or features can be observed in the CL map of the peak energy [Fig. 1(i)]. Similar observations from hexagons and their surrounding areas have been reported previously in Ref. 36. It is proposed that during the growth of the hexagonal features dislocations inside may bend toward the edges of the hexagons or annihilate, leading to a reduced dislocation density on top of the hexagons.

The crystallographic properties of the hexagons were investigated using EBSD. First, the crystal polarity was determined from EBSD maps recorded from a region on top of the hexagon and one from the surrounding area. Here, the experimental EBSPs were compared with dynamically simulated patterns of N-polar and Ga-polar orientation following the methodology in Refs. 37 and 38. In summary, although the symmetry of the material does not change, an inversion around the polar c-axis leads to subtle intensity changes of the Kikuchi band edges, which can be detected via a cross-correlation against simulations. From this analysis, it could be confirmed that the hexagonal features and the surrounding planar regions were of N-polar orientation as seen in the inverse pole figures along the Z direction (sample normal direction) as shown in Fig. S2 in the supplementary material.

Next, the elastic strain on the sample surface was determined from the EBSD measurements across a hexagon, displayed in the SE image in Fig. 2(g). The normal strain components ε_{xx}, ε_{yy} and ε_{zz} are shown in Figs. 2(a), 2(e), and 2(i), respectively, and the shear strain components ε_{xy}, ε_{xz}, and ε_{yz} in Figs. 2(b), 2(c), and 2(f), respectively. All strain components are displayed on the same scale [Fig. 2(h)] for better comparison. Each strain map is normalized to the mean of the map, meaning the mean was subtracted so that the strain distribution is centered around zero. The strain components are expressed with respect to the sample reference frame directions X, Y, and Z. Here, the reference directions are chosen to align with the $\langle 11\bar{2}0 \rangle$, $\langle 1\bar{1}00 \rangle$ and $[000\bar{1}]$ directions (a-, m-, and $-c$ directions) of the hexagonal wurtzite lattice as shown in Fig. 2(d).

It can immediately be seen that the hexagon is split into triangular segments with opposite segments showing the same behavior (giving a bow-tie shape), except the ε_{zz} component [Fig. 2(i)], which changes radially from the center to the edges. The ε_{xx} component in Fig. 2(a) shows two segments, one at the top and one at the bottom, under dominant tensile strain (red). For these two segments the sidewall of the $\{1\bar{1}00\}$-plane is aligned with the X sample reference frame direction. It can also be seen that this tensile strain component increases radially from the center to the edge of the hexagon (change from lighter to darker red). The ε_{yy}

component for these two segments on the other hand shows compression (blue). It can be interpreted that these two segments are elongated in the X direction and compressed in the Y with increasing distance from the center of the hexagonal feature. The ε_{yy} component in Fig. 2(e) shows four segments being under dominant tensile strain, two on the left side and two on the right. For these segments the side walls do not exactly line up with the Y sample reference frame direction, but are at 30° to it. Nonetheless, these segments exhibit elongation along the Y direction, but the magnitude is slightly less than that observed for the top and bottom segment in the X direction. Again, the tensile strain increases from the center to the edges. The ε_{xx} component for those four segments shows much less tension; toward the center, there is even compression. Overall, this suggests that the hexagons are under tensile strain, which is predominantly parallel to the six sides of the hexagon. Additionally, this tensile strain increases with increasing distance from the center of the hexagon.

To further investigate the impact of the sample frame reference system on the results of the strain analysis, EBSD was performed on the same hexagon where the sample was rotated by 30° and 90° with respect to the initial measurement as shown in the SE images in Fig. S3 in the supplementary material. All strain results of this rotation series are shown in Fig. S4 in the supplementary material. The initial measurement geometry in Figs. S3 and S4 in the supplementary material is the same as shown above in Fig. 2 such that the X and Y directions align with the $\langle 11\bar{2}0 \rangle$ and $\langle 1\bar{1}00 \rangle$ directions of the wurtzite lattice, respectively. For the measurements after a rotation of 30° and 90° these orientations swap around and the X and Y directions align with the $\langle 1\bar{1}00 \rangle$ and $\langle 11\bar{2}0 \rangle$ directions, respectively. In the first case, we can see the impact of a different crystallographic alignments with respect to the sample reference frame system (initial measurement vs 30° rotation). The second case allows us to investigate the symmetry of the hexagon whereby we measure under the same crystallographic alignment but with a relative rotation of 60° of the hexagon so that another direction of the same family aligns with the sample reference frame system (30° and 90° rotation).

First, we look at the case where the hexagon is rotated by 30° compared with the initial alignment. In this case, the $\langle 1\bar{1}00 \rangle$ and $\langle 11\bar{2}0 \rangle$ directions swap around with respect to the fixed X and Y sample reference frame directions. The initial strain results are shown in Figs. S3(a)–S3(f) in the supplementary material and after 30° rotation in Figs. S3(g)–S3(l) in the supplementary material. The interesting strain components are ε_{xx} and ε_{yy}, which have to be interrogated together. In the initial orientation, only two triangular segments with $\langle 1\bar{1}00 \rangle$ sides or edges are parallel with the X direction, that is, the top and bottom. These two segments show tensile strain (red) in the ε_{xx} [Fig. S4(a) in the supplementary material] component as observed previously in Fig. 2(a). After 30° rotation, the two segments that are now parallel to one of the sample reference frame directions are the segments on the left and right with the $\langle 1\bar{1}00 \rangle$ sides parallel to the Y direction. In this case, the tensile strain occurs in the ε_{yy} component in Fig. S4(h) in the supplementary material. A similar swapping behavior is observed for the strain shown in Figs. S4(b) and S4(g) in the supplementary material. The normal strain components ε_{zz} remain the same after rotating 30° [Figs. S3(c) and S3(i) in the supplementary material].
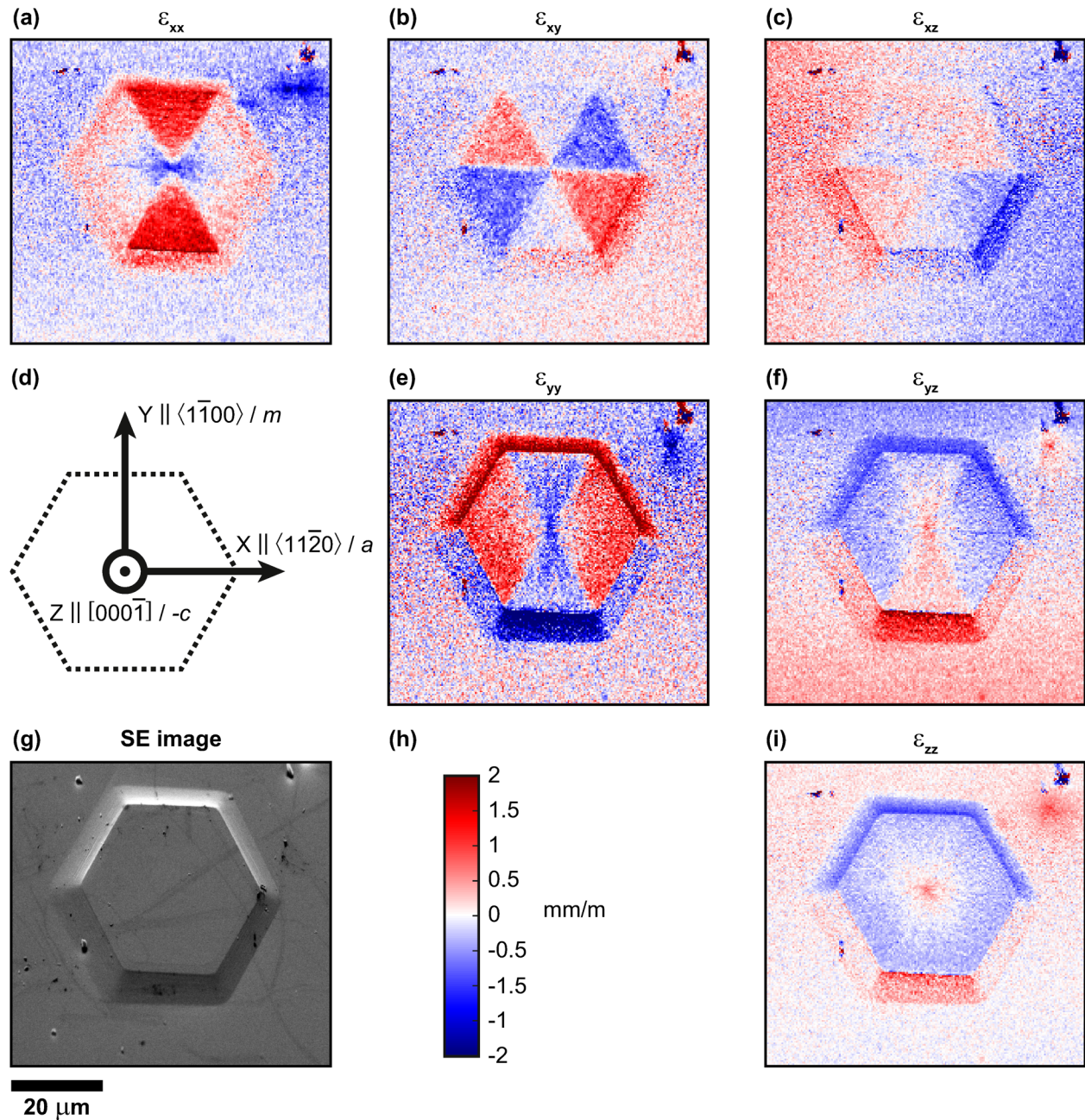
FIG. 2. EBSD: Normal strain components (a) ε_{xx}, (e) ε_{yy}, and (i) ε_{zz} and shear strain components (b) ε_{xy}, (c) ε_{xz}, and (f) ε_{yz} from the hexagon shown in the (g) SE image. (h) The color scale is normalized to the mean of each image for better comparison of each map. All strain components are plotted on the same scale. (d) Crystallographic directions and their relationship with the sample reference frame directions X, Y, and Z. The 2D unit cell is shown in dashed lines. All images are shown on the same spatial scale.

Next, the sample is rotated a further 60° after the 30° rotation, and we compare the two the strain results after both rotations, which are shown in Figs. S3(g)–S3(l) and Figs. S3(m)–S3(r) in the supplementary material. In both cases, the crystallographic alignment of the hexagon with respect to the sample reference frame is the same, except that the hexagon and each triangular segment is rotated by 60°. It can immediately be seen that the strain maps for each strain component show the same behavior
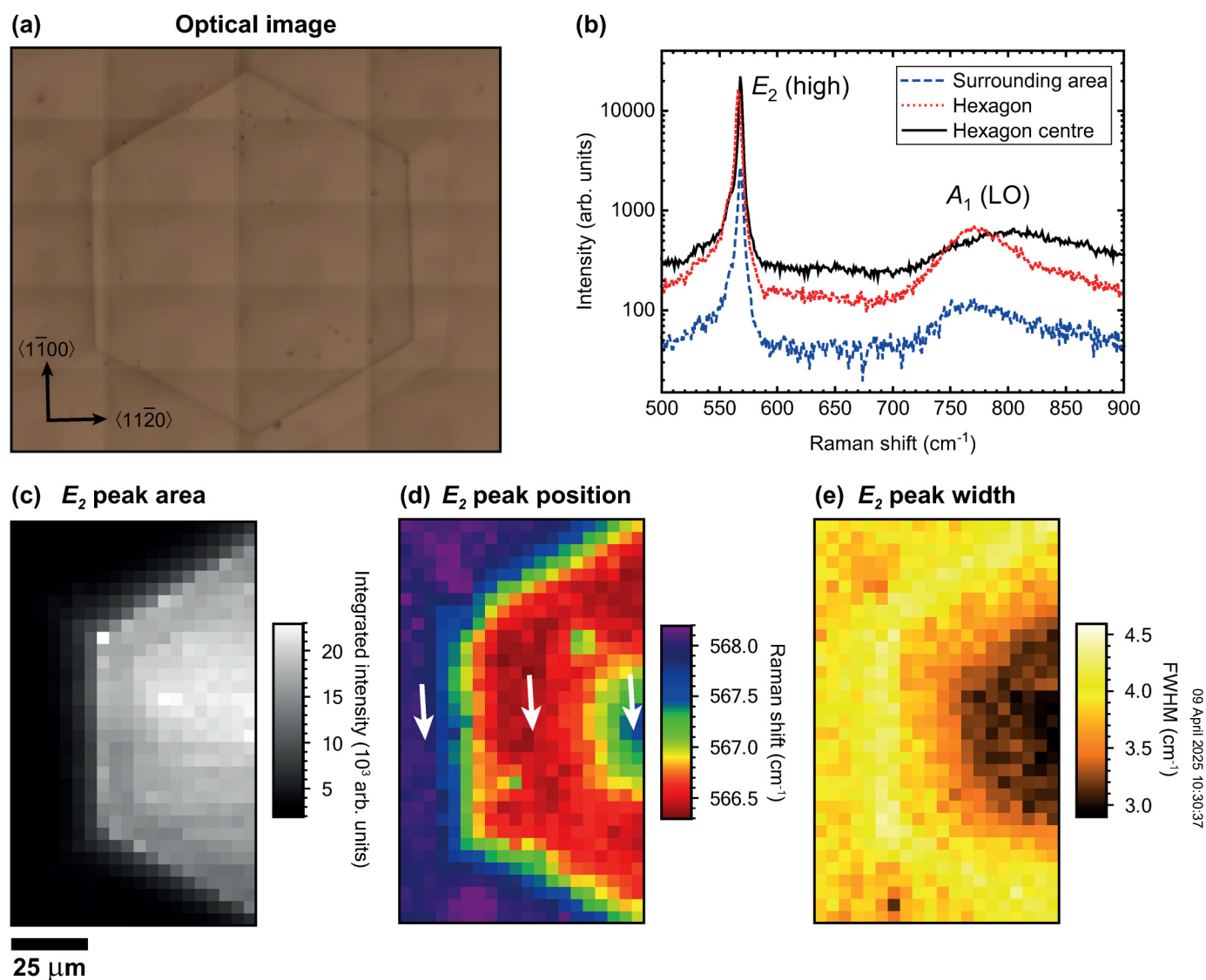
FIG. 3. Raman imaging: (a) Optical image of the measured hexagon. (b) Example Raman spectra from selected spots as marked by white arrows in the peak position map in (d). Raman maps of the (c) peak area, (d) peak position, and (e) peak width (FWHM) of the E_2 (high) Raman mode. All images are shown on the same spatial scale.

after 60° rotation. It is important to note that the strain distribution, i.e., the colors in the image, does not rotate.

From the results of the rotation series, it can be inferred that the strain state of each of the triangular segments is the same. In summary, the hexagons are composed of equivalent triangular segments with tensile strain along symmetrically equivalent $\langle 11\bar{2}0 \rangle$ directions, parallel to the sides of the hexagons. This tensile strain also radially increases with distance from the center of the hexagon. This implies that the strain properties also possesses a hexagonal symmetry and the pattern shown in each of the strain maps is an artifact of the Cartesian coordinate system used for the strain

tensor. Therefore, careful analysis is required for materials with hexagonal symmetry.

Finally, we investigate a series of hexagons, Fig. S5 in the supplementary material, in the same crystallographic orientation with respect to the sample reference frame to understand if all hexagonal features behave similarly. All EBSD strain maps from four different hexagons are displayed in Fig. S6 in the supplementary material. The measured hexagons are also differing in size from about 50 to $100\,\mu$m. Overall, all measured hexagons show a similar strain behavior. There are some differences, but the relative strain behavior is similar. The differences are attributed to the general

appearance of the hexagons. The first hexagon in Fig. S5(a) in the supplementary material shows additional hexagonal terraces, whereas hexagons 2 and 3 [Figs. S5(b) and S5(c) in the supplementary material] have fairly long sloping down sidewalls from the edges and hexagon 4 [Fig. S5(d) in the supplementary material] possesses relatively short sidewalls. It also becomes more obvious in the strain maps that there is an additional, possibly buried, hexagon near hexagon 1 and hexagon 3. The strain field of the additional hexagons is superimposed on the main hexagonal feature.

Another approach to infer information on stress and strain is Raman spectroscopy. In GaN, the Raman E_2 (high) phonon mode is influenced by variations in stress and strain.[39] Here, we use micro-Raman mapping to investigate changes in the E_2 (high) mode across a hexagon as shown in the optical image in Fig. 3(a). The peak area, peak position (Raman shift), and FWHM of the E_2 (high) mode are shown in Figs. 3(c)–3(e), respectively.

In the case of hexagonal features in GaN samples studied here, EBSD showed a presence of pronounced patterns in the planar strain distributions as shown in Fig. 2. These strain variations of the order of 2×10^{-3} (or 2 mm/m), particularly in the ε_{xx}, ε_{yy}, and ε_{xy} components, should also influence the Raman spectra sensitive to strain. The peak position map of the Raman mode in Fig. 3(d) shows a radially symmetrical strain profile of the GaN hexagon. The measured peak position in the surrounding area is about 568.1 cm^{-1}, while on the majority of the top of the hexagons, it reduces to around 566.4 cm^{-1}; examples of Raman spectra are shown in Fig. 3(b). Note that these values fluctuated from hexagon to hexagon, and this is just a representative value. The phonon frequencies in unstrained GaN material can vary with layer thickness, orientation, growth method etc., making precise determination of absolute strain from only Raman measurements uncertain.[40–43] For stress-free GaN on sapphire, the values for the E_2 (high) phonon mode are around 566.8 cm^{-1}. The observed shift of the Raman peak of 1.7 cm^{-1} from the top (or the main body) of the hexagon to the surrounding area means that the area around the thicker hexagons is compressively strained with respect to the near strain-free hexagon after the growth. This increase in strain can also be correlated to the higher threading dislocation density away from the hexagons observed in CL in Fig. 1.[44,45] Additionally, the Raman peak at the center of the hexagon is shifted to a higher frequency with respect to the main body of the hexagon, meaning that the center is compressively strained. The Raman map in Fig. 3(d) shows that the strain reduces from the center of the hexagon to its edge. This agrees very well with the findings from EBSD above, where it was found that the hexagons have greater tensile strain toward the sides relative to the center, which is equivalent to a reduction in compressive strain as seen in Raman. Similar strain observations have been reported previously in Ref. 36.

Reduced intensity and increased peak width are indicators for areas of reduced material quality with higher threading dislocation density. This can be observed in Figs. 3(c) and 3(e) where the intensity drops off and the width increases from 2.8 cm^{-1} on top of the hexagon to 4.1 cm^{-1} in the surrounding region. This agrees well with the findings from CL imaging [Figs. 1(d), 1(e), and 1(f)] with decreased CL intensity in the surrounding area with increased defect densities. This confirms that the crystalline quality of the hexagonal feature is greatly improved compared with its surrounding matrix.

Overall, CL imaging showed a reduction of dislocation density on top of the hillocks compared with the highly defected surrounding region. EBSD and Raman imaging showed that the hexagon is overall more relaxed compared with the compressively strained surrounding material. Furthermore, it was found that the hexagon exhibits more tensile strain toward the sides or edges compared to the center. As mentioned previously, it has been proposed that during the growth of the hexagon, dislocations may bend toward the sides of the hexagon and annihilate leading to the observed reduced dislocation density on top of the hexagons.[36] It is also known that dislocation annihilation in compressively strained GaN causes a reduction in compressive strain and even a transition to tensile strain.[46–48] The AFM data in Figure S1 shows that the hexagonal hillocks are not flat on top, but the height is linearly increasing from the side to the center. This increase in height toward the center may also contribute to the observed tensile strain relaxation toward the center.

IV. CONCLUSION

In summary, we investigated the crystallographic and light emission properties of hexagonal hillocks in N-polar GaN using EBSD, CL imaging, and Raman mapping. Although these hexagons are not desired and increase the surface roughness, CL imaging revealed that they exhibit improved optical characteristics compared with their surrounding material. Not only is the emission intensity increased on top of the hexagons, but also threading dislocations can clearly be resolved as dark spots in CL intensity images. In the planar surrounding material, there is a great density of dark spots, which is attributed to a very high density of defects in that area. Extensive strain analysis using EBSD revealed that the hexagons are composed of equivalent triangular segments with tensile strain along symmetrically equivalent $\langle 11\bar{2}0 \rangle$ directions, which is parallel to the sides of the hexagons. The tensile strain also radially increases with distance from the center of the hexagon. The observations from CL and EBSD were supported by Raman mapping of the E_2 (high) mode. This offers valuable insights into the strain and luminescence state of these hexagonal features, aiding in the enhancement of material quality and devices.

SUPPLEMENTARY MATERIAL

See the supplementary material for measurement of hexagon topography (S1), the determination of crystal polarity (S2), rotation series of a single hexagon (S3), and strain determination of four hexagons in the same alignment (S4).

ACKNOWLEDGMENTS

09 April 2025 10:30:37

to thank Dr. Graham Meaden (BLG Vantage) for the very useful discussions regarding the strain analysis.

DATA AVAILABILITY

The data associated with this research are available at https://doi.org/10.15129/36f7db3e-5a2d-4e97-91e6-e6e55e973a7b or from the corresponding author.

REFERENCES

[1]M. Stutzmann, O. Ambacher, M. Eickhoff, U. Karrer, A. Lima Pimenta, R. Neuberger, J. Schalwig, R. Dimitrov, P. Schuck, and R. Grober, "Playing with polarity," Phys. Status Solidi B **228**, 505 (2001).

[2]S. Keller, H. Li, M. Laurent, Y. Hu, N. Pfaff, J. Lu, D. F. Brown, N. A. Fichtenbaum, J. S. Speck, S. P. DenBaars, and U. K. Mishra, "Recent progress in metal-organic chemical vapor deposition of (000$\bar{1}$) N-polar group-III nitrides," Semicond. Sci. Technol. **29**, 113001 (2014).

[3]S. Mohanty, K. Khan, and E. Ahmadi, "N-polar GaN: Epitaxy, properties, and device applications," Prog. Quantum Electron. **87**, 100450 (2023).

[4]M. H. Wong, S. Keller, S. D. Nidhi, D. J. Denninghoff, S. Kolluri, D. F. Brown, J. Lu, N. A. Fichtenbaum, E. Ahmadi, U. Singisetti, A. Chini, S. Rajan, S. P. DenBaars, J. S. Speck, and U. K. Mishra, "N-polar GaN epitaxy and high electron mobility transistors," Semicond. Sci. Technol. **28**, 074009 (2013).

[5]O. S. Koksaldi, J. Haller, H. Li, B. Romanczyk, M. Guidry, S. Wienecke, S. Keller, and U. K. Mishra, "N-polar GaN HEMTs exhibiting record breakdown voltage over 2000 V and low dynamic on-resistance," IEEE Electron Device Lett. **39**, 1014 (2018).

[6]S. Fuke, H. Teshigawara, K. Kuwahara, Y. Takano, T. Ito, M. Yanagihara, and K. Ohtsuka, "Influences of initial nitridation and buffer layer deposition on the morphology of a (0001) GaN layer grown on sapphire substrates," J. Appl. Phys. **83**, 764 (1998).

[7]T. Zywietz, J. Neugebauer, and M. Scheffler, "Adatom diffusion at GaN (0001) and (000$\bar{1}$) surfaces," Appl. Phys. Lett. **73**, 487 (1998).

[8]J. Weyher, P. Brown, A. Zauner, S. Müller, C. Boothroyd, D. Foord, P. Hageman, C. Humphreys, P. Larsen, I. Grzegory, and S. Porowski, "Morphological and structural characteristics of homoepitaxial GaN grown by metalorganic chemical vapour deposition (MOCVD)," J. Cryst. Growth **204**, 419 (1999).

[9]S. Keller, N. Fichtenbaum, F. Wu, G. Lee, S. P. DenBaars, J. S. Speck, and U. K. Mishra, "Effect of the nucleation conditions on the polarity of AlN and GaN films grown on C-face 6H–SiC," Jpn. J. Appl. Phys. **45**, L322 (2006).

[10]T. Matsuoka, Y. Kobayashi, H. Takahata, T. Mitate, S. Mizuno, A. Sasaki, M. Yoshimoto, T. Ohnishi, and M. Sumiya, "N-polarity GaN on sapphire substrate grown by MOVPE," Phys. Status Solidi B **243**, 1446 (2006).

[11]A. Zauner, J. Weyher, M. Plomp, V. Kirilyuk, I. Grzegory, W. van Enckevort, J. Schermer, P. Hageman, and P. Larsen, "Homo-epitaxial GaN growth on exact and misoriented single crystals: Suppression of hillock formation," J. Cryst. Growth **210**, 435 (2000).

[12]M. Sumiya, K. Yoshimura, T. Ito, K. Ohtsuka, S. Fuke, K. Mizuno, M. Yoshimoto, H. Koinuma, A. Ohtomo, and M. Kawasaki, "Growth mode and surface morphology of a GaN film deposited along the N-face polar direction on c-plane sapphire substrate," J. Appl. Phys. **88**, 1158 (2000).

[13]S. Keller, N. A. Fichtenbaum, F. Wu, D. Brown, A. Rosales, S. P. DenBaars, J. S. Speck, and U. K. Mishra, "Influence of the substrate misorientation on the properties of N-polar GaN films grown by metal organic chemical vapor deposition," J. Appl. Phys. **102**, 083546 (2007).

[14]S. Mita, R. Collazo, A. Rice, J. Tweedie, J. Xie, R. Dalmau, and Z. Sitar, "Impact of gallium supersaturation on the growth of N-polar GaN," Phys. Status Solidi C **8**, 2078 (2011).

[15]T. Aisaka, T. Tanikawa, T. Kimura, K. Shojiki, T. Hanada, R. Katayama, and T. Matsuoka, "Improvement of surface morphology of nitrogen-polar GaN by introducing indium surfactant during MOVPE growth," Jpn. J. Appl. Phys. **53**, 085501 (2014).

[16]M. Pristovsek, I. Furuhashi, and P. Pampili, "Growth of n-polar (0001-) GaN in metal–organic vapour phase epitaxy on sapphire," Crystals **13**, 1072 (2023).

[17]S. Mohn, N. Stolyarchuk, T. Markurt, R. Kirste, M. P. Hoffmann, R. Collazo, A. Courville, R. Di Felice, Z. Sitar, P. Vennéguès, and M. Albrecht, "Polarity control in group-III nitrides beyond pragmatism," Phys. Rev. Appl. **5**, 054004 (2016).

[18]H. Zhang, P. P. Paskov, O. Kordina, J.-T. Chen, and V. Darakchieva, "N-polar AlN nucleation layers grown by hot-wall MOCVD on SiC: Effects of substrate orientation on the polarity, surface morphology and crystal quality," Phys. B **580**, 411819 (2020).

[19]T. Tanikawa, S. Kuboya, and T. Matsuoka, "Control of impurity concentration in N-polar (000-1) GaN grown by metalorganic vapor phase epitaxy," Phys. Status Solidi B **254**, 1600751 (2017).

[20]P. Pampili, V. Z. Zubialevich, and P. J. Parbrook, "Geometrically controlled microscale patterning and epitaxial lateral overgrowth of nitrogen-polar GaN," Cryst. Growth Des. **24**, 6095 (2024).

[21]H. Zhang, T. Chen, A. Papamichail, I. Persson, P. P. Paskov, and V. Darakchieva, "High-quality N-polar GaN optimization by multi-step temperature growth process," J. Cryst. Growth **603**, 127002 (2023).

[22]A. Winkelmann, C. Trager-Cowan, F. Sweeney, A. P. Day, and P. Parbrook, "Many-beam dynamical simulation of electron backscatter diffraction patterns," Ultramicroscopy **107**, 414 (2007).

[23]G. Nolze, M. Jürgens, J. Olbricht, and A. Winkelmann, "Improving the precision of orientation measurements from technical materials via EBSD pattern matching," Acta Mater. **159**, 408 (2018).

[24]F. Bachmann, R. Hielscher, and H. Schaeben, "Texture analysis with MTEX—Free and open source software toolbox," Solid State Phenom. **160**, 63 (2010).

[25]A. J. Wilkinson, G. Meaden, and D. J. Dingley, "High-resolution elastic strain measurement from electron backscatter diffraction patterns: New levels of sensitivity," Ultramicroscopy **106**, 307 (2006).

[26]T. Britton and A. Wilkinson, "High resolution electron backscatter diffraction measurements of elastic strain variations in the presence of larger lattice rotations," Ultramicroscopy **114**, 82 (2012).

[27]J. Bruckbauer, P. R. Edwards, T. Wang, and R. W. Martin, "High resolution cathodoluminescence hyperspectral imaging of surface features in InGaN/GaN multiple quantum well structures," Appl. Phys. Lett. **98**, 141908 (2011).

09 April 2025 10:30:37

[28]P. R. Edwards, L. K. Jagadamma, J. Bruckbauer, C. Liu, P. Shields, D. Allsopp, T. Wang, and R. W. Martin, "High-resolution cathodoluminescence hyperspectral imaging of nitride nanostructures," Microsc. Microanal. **18**, 1212 (2012).

[29]S. J. Rosner, E. C. Carr, M. J. Ludowise, G. Girolami, and H. I. Erikson, "Correlation of cathodoluminescence inhomogeneity with microstructural defects in epitaxial GaN grown by metalorganic chemical-vapor deposition," Appl. Phys. Lett. **70**, 420 (1997).

[30]G. Naresh-Kumar, J. Bruckbauer, P. R. Edwards, S. Kraeusel, B. Hourahine, R. W. Martin, M. J. Kappers, M. A. Moram, S. Lovelock, R. A. Oliver, C. J. Humphreys, and C. Trager-Cowan, "Coincident electron channeling and cathodoluminescence studies of threading dislocations in GaN," Microsc. Microanal. **20**, 55 (2014).

[31]N. Gmeinwieser, P. Gottfriedsen, U. T. Schwarz, W. Wegscheider, R. Clos, A. Krtschil, A. Krost, A. Weimar, G. Brüderl, A. Lell, and V. Härle, "Local strain and potential distribution induced by single dislocations in GaN," J. Appl. Phys. **98**, 116102 (2005).

[32]C. Netzel, A. Knauer, F. Brunner, A. Mogilatenko, and M. Weyers, "Temperature dependence of dark spot diameters in GaN and AlGaN," Phys. Status Solidi B **258**, 2100358 (2021).

[33]J. Lähnemann, V. M. Kaganer, K. K. Sabelfeld, A. E. Kireeva, U. Jahn, C. Chèze, R. Calarco, and O. Brandt, "Carrier diffusion in GaN: A cathodoluminescence study. III. Nature of nonradiative recombination at threading dislocations," Phys. Rev. Appl. **17**, 024019 (2022).

[34]I.-H. Lee, J. J. Lee, P. Kung, F. J. Sanchez, and M. Razeghi, "Band-gap narrowing and potential fluctuation in Si-doped GaN," Appl. Phys. Lett. **74**, 102 (1999).

[35]S. L. Rhode, M. K. Horton, W. Y. Fu, S.-L. Sahonta, M. J. Kappers, T. J. Pennycook, C. J. Humphreys, R. O. Dusane, and M. A. Moram, "Dislocation core structures in Si-doped GaN," Appl. Phys. Lett. **107**, 243104 (2015).

[36]T. Jiang, Z. Lin, J. Zhang, S. Xu, J. Huang, M. Niu, X. Gao, L. Guo, and Y. Hao, "Raman mapping of hexagonal hillocks in N-polar GaN grown on c-plane sapphire," Superlattices Microstruct. **104**, 162 (2017).

[37]A. Winkelmann, G. Nolze, M. Himmerlich, V. Lebedev, and A. Reichmann, "Point-group sensitive orientation mapping using EBSD," in *Proceedings of the 6th International Conference on Recrystallization and Grain Growth (ReX&GG 2016)* (Springer, Cham, 2016), p. 281.

[39]A. Sarua, M. Kuball, and J. E. Van Nostrand, "Phonon deformation potentials of the E_2 (high) phonon mode of $Al_xGa_{1-x}N$," Appl. Phys. Lett. **85**, 2217 (2004).

[40]C. Kisielowski, J. Krüger, S. Ruvimov, T. Suski, J. W. Ager, E. Jones, Z. Liliental-Weber, M. Rubin, E. R. Weber, M. D. Bremser, and R. F. Davis, "Strain-related phenomena in GaN thin films," Phys. Rev. B **54**, 17745 (1996).

[41]V. Y. Davydov, Y. E. Kitaev, I. N. Goncharuk, A. N. Smirnov, J. Graul, O. Semchinova, D. Uffmann, M. B. Smirnov, A. P. Mirgorodsky, and R. A. Evarestov, "Phonon dispersion and Raman scattering in hexagonal GaN and AlN," Phys. Rev. B **58**, 12899 (1998).

[42]S. Tripathy, S. J. Chua, P. Chen, and Z. L. Miao, "Micro-Raman investigation of strain in GaN and $Al_xGa_{1-x}N$/GaN heterostructures grown on Si(111)," J. Appl. Phys. **92**, 3503 (2002).

[43]P. Puech, F. Demangeot, J. Frandon, C. Pinquier, M. Kuball, V. Domnich, and Y. Gogotsi, "GaN nanoindentation: A micro-Raman spectroscopy study of local strain fields," J. Appl. Phys. **96**, 2853 (2004).

[44]G. Nootz, A. Schulte, L. Chernyak, A. Osinsky, J. Jasinski, M. Benamara, and Z. Liliental-Weber, "Correlations between spatially resolved Raman shifts and dislocation density in GaN films," Appl. Phys. Lett. **80**, 1355 (2002).

[45]T. Kitamura, S. Nakashima, N. Nakamura, K. Furuta, and H. Okumura, "Raman scattering analysis of GaN with various dislocation densities," Phys. Status Solidi C **5**, 1789 (2008).

[46]A. E. Romanov and J. S. Speck, "Stress relaxation in mismatched layers due to threading dislocation inclination," Appl. Phys. Lett. **83**, 2569 (2003).

[47]M. A. Moram, M. J. Kappers, F. Massabuau, R. A. Oliver, and C. J. Humphreys, "The effects of Si doping on dislocation movement and tensile stress in GaN films," J. Appl. Phys. **109**, 073509 (2011).

[48]S. Raghavan, I. C. Manning, X. Weng, and J. M. Redwing, "Dislocation bending and tensile stress generation in GaN and AlGaN films," J. Cryst. Growth **359**, 35 (2012).

09 April 2025 10:30:37